Effect of Critical Tempering on Microstructure Evolution, Mechanical Performance, and Corrosion Behavior of a Cast Multiphase Stainless Steel

Jing-yu He 1 and *Xiang Chen2

- 1. School of Materials Science and Engineering, Tsinghua University, Beijing 100084, China
- 2. Key Laboratory for Advanced Materials Processing Technology, Ministry of Education, Beijing 100084, China
 - 3. *Corresponding address: e-mail: xchen@tsinghua.edu.cn

Abstract: A novel cast stainless steel with an engineered multiphase microstructure was systematically investigated in this work. Following solution treatment at 1050° C and water quenching, the specimens were subjected to further tempering at 570° C, 610° C, and 650° C to explore the effects of critical tempering on microstructure, mechanical properties, and corrosion resistance. Various characterization techniques were employed to examine the phase distribution within the microstructure, with particular attention given to the content and morphology of reversed austenite. Tensile and corrosion tests were carried out to evaluate the performance of the specimens. The results revealed that critical tempering significantly enhanced the mechanical properties, with the ST610 specimen achieving the highest product of strength and elongation (PSE = 23.6 GPa • %), whereas corrosion resistance deteriorated with increasing tempering temperature. Calculations of the martensite start temperature (Ms) and stacking fault energy (SFE) for the reversed austenite in different specimens indicated that the stability of reversed austenite strongly influences mechanical behavior through the TRIP and TWIP effects. However, tempering-induced Cr segregation at ferrite/martensite interfaces and the formation of Cr-depleted zones, which became more pronounced at higher tempering temperatures, led to a degradation in corrosion resistance. Furthermore, the process of multiphase coordinated deformation and corrosion initiation in the multiphase stainless steel were also investigated in this paper.

Keywords: Cast Stainless Steel; Multiphase Structure; Stability of Reverted Austenite; TRIP and TWIP; Corrosion Resistance

1 Introduction

With the growing demand for enhanced mechanical performance in steels and the challenge of overcoming traditional strength-ductility trade-off, construction of multiphase, multiscale, and metastable (M³) microstructures has become an increasingly popular strategy among researchers in recent years^[1]. Compared with single-phase ferritic or austenitic stainless steels, duplex stainless steels exhibit superior strength and corrosion resistance. Additionally, martensitic precipitation-hardened stainless steels offer better comprehensive properties than conventional martensitic steels. Therefore, the development of multiphase stainless steels presents a promising research direction.

Several studies have demonstrated the potential of multiphase stainless steels. Sérgio S.M. *et al.* reported a martensite-based triphase stainless steel containing 37% ferrite and 7.4% reverted austenite, achieving an ultimate

tensile strength exceeding 800 MPa along with elongation over 20% ^[2,3]. Menghao Liu *et al.* further increased the Ni content to enhance the austenite fraction, achieving elongations beyond 36%, and conducted detailed investigations into the corrosion and hydrogen embrittlement behaviors ^[4,5].

Building upon these advances, Wu *et al.* in our group developed a novel triphase stainless steel based on the PH13-8 martensitic precipitation-hardened system by introducing ferrite through high Si addition and forming reverted austenite via critical tempering after quenching. The resulting steel exhibited an ultimate tensile strength greater than 1000 MPa and elongation exceeding 15%^[6-8]. Silicon not only provides substantial solid solution strengthening but also synergizes with chromium to promote the formation of a stable oxide passive film on the steel surface, thus positively influencing both mechanical properties and corrosion resistance^[9-11].

The stabilization of reverted austenite generated during tempering plays a pivotal role in enhancing the comprehensive performance of multiphase stainless improves Reverted austenite mechanical properties through transformation-induced plasticity and twinning-induced plasticity mechanisms^[12-14]. The stability of retained austenite has been extensively studied in martensitic stainless steels. Xilin Xiong et al. achieved improved strength and elongation in 15Cr supermartensitic stainless steel through annealing below the transformation temperature to stabilize austenite^[15]. Similarly, Chan He et al. enhanced the elongation of 13Cr supermartensitic stainless steel to over 20% by incorporating nitrogen and employing an innovative heat treatment known as QAP, which combines intercritical annealing (A) with quenching and partitioning (QP)^[16]. On the other hand, Peng Wang and Yonggang Zhao independently demonstrated that the presence of reverted austenite after tempering significantly increases the passive film thickness, thereby improving the corrosion resistance of 13Cr supermartensitic stainless steels^[17,18].

Although high-Si multiphase stainless steels also maintain martensite as the primary matrix, introduction of ferrite creates a microstructural duality that could alter tempering behavior in ways not yet fully characterized, presenting critical opportunities for materials science research. Thus, it is necessary to systematically investigate the effects of tempering on the microstructure and properties of multiphase stainless steels to optimize heat treatment strategies and fully realize their performance potential. In this study, a newly designed cast multiphase stainless steel was employed to systematically explore the effects of critical tempering (570°C, 610°C, and 650°C) on microstructural evolution, reverted austenite stability, mechanical properties, and corrosion behavior. The deformation mechanisms and corrosion processes were further elucidated from a composition-microstructure-property perspective.

2 Experiments and Methods

In this study, a cast stainless steel was specifically designed with a multiphase microstructure by balancing strength, toughness, and corrosion resistance. The nominal composition of the designed alloy is detailed in Table 1. The alloying elements were selected to optimize austenite phase stability (Ni, Mn), enhance matrix strengthening (Si, Ni, Al, Cu), and improve corrosion resistance (Cr, Mo, Si). Ingots (~5 kg) were produced by vacuum induction melting, homogenized at 1050°C for 1 h, and water-quenched to reduce segregation. Due to the

ferrite-stabilizing effect of Si, δ -ferrite remained in the solution-treated sample (designated S1050). Subsequent tempering at 570°C, 610°C, and 650°C yielded ST570, ST610, and ST650, respectively (Fig. 1)

The δ -ferrite in stainless steels is difficult to eliminate through heat treatments below 950°C^[19], resulting in its presence in the microstructure. Following critical tempering, a portion of reverted austenite formed, resulting in a triphase microstructure consisting of ferrite, martensite, and austenite in the ST specimens. The specimens were ground, mechanically polished, and subsequently etched according to the method proposed by Lichtenegger and Bloech^[20] to visualize δ -ferrite. The δ -ferrite volume fraction was quantified by analyzing optical micrographs at 500× magnification with ImageJ software.

Microstructural characterization was conducted using optical microscopy (OM), scanning electron microscopy electron backscatter diffraction (EBSD), transmission electron microscopy (TEM) and X-ray diffraction (XRD). Optical micrographs were captured using a ZEISS Gemini 2 microscope. SEM and EBSD were performed using a TESCAN S9000X system; Specimens for SEM observation were polished and then etched in a 15% HCl-FeCl₃ solution, while EBSD specimens were prepared by electrochemical polishing (10% HClO₄ + 90% CH₃COOH, 20–25 V, 0.05 mA). EBSD data were analyzed with AZtecCrystal to obtain phase distribution maps, band contrast (BC) maps, kernel average misorientation (KAM) maps, and grain boundary (GB) maps. TEM foils were thinned to ~50 μm, punched into 3 mm disks, and ion-milled using 4 kV Ar⁺ ions at 7-8°, with observations conducted on a JEM-2100 microscope. The XRD patterns were refined using the Rietveld method implemented in Maud software to determine the volume fraction of austenite. Additionally, Thermo-Calc software with the TCFE 12 database was employed to predict the volume fraction and chemical composition of austenite. These predicted compositions were used to calculate the martensite start temperature (Ms) and the stacking fault energy (SFE) of the austenite phase.

Tensile tests were carried out on dog-bone specimens (25 mm gauge length, 5 mm diameter) using an MTS810 machine at a strain rate of 1×10⁻³s⁻¹. After fracture, approximately 5 mm × 5 mm square sections were extracted from the fracture zone for post-deformation microstructural analysis. For corrosion resistance evaluation, specimens (50 mm ×30 mm ×5 mm) were immersed in a 6% FeCl₃–HCl solution at 50°C for 24

hours. Mass loss was determined by weighing the samples before and after immersion to calculate the corrosion rate. In addition, linear potentiodynamic polarization tests were performed in a 1 M NaCl solution at 25°C (sweep rate: 0.5 mV/s) using a Corrtest CS2350H electrochemical workstation.

Table 1 the chemical compositions of the experimental steel (wt. %).

С	Si	Mn	Cr	Ni	Mo	Cu	Al	Fe
0.02	2.5	1.0	13.4	6.8	0.9	1.1	0.3	Bala
4	8	8	8	9	7	1	5	nce

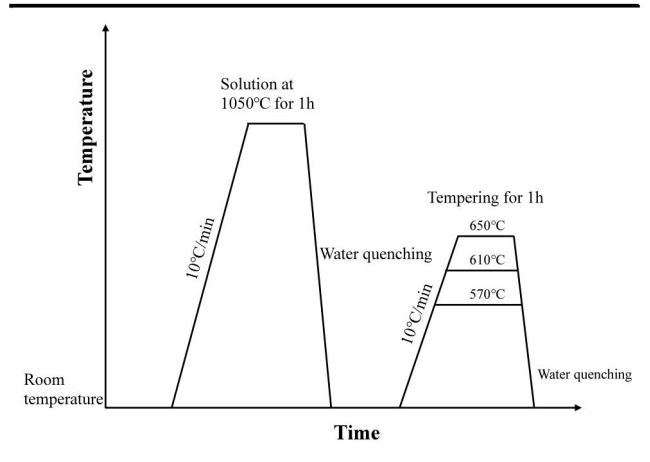


Fig. 1. Heat treatment procedure schematic for the experimental steel

3. Results

3.1 Microstructure of the experimental steel under various treatments

Fig. 2(a) illustrates the phase fractions of the experimental steel as a function of temperature under equilibrium conditions, omitting phases below 0.5% for clarity. Due to the extremely low carbon content, the martensite formed in the microstructure exhibits a body-centered cubic (BCC) structure. The presence of Mo and Si promotes the precipitation of the Laves phase at temperatures below 750°C. The phase diagram indicates that under equilibrium conditions, δ -ferrite would fully transform into austenite at approximately 1300°C. However, owing to the high silicon content (~2.6 wt.%), during the peritectic reaction $(L+\delta \rightarrow \gamma)$ in the casting process, ferrite-stabilizing elements such as Si and Cr tend to enrich in both the liquid and δ -ferrite phases. This enrichment reduces the chemical driving force for the $\delta \rightarrow \gamma$ transformation^[21], leading to the retention of δ -ferrite from high-temperature states in the final microstructure, as observed in Fig. 3(a). Fig. 2(b) presents a magnified view of the critical tempering temperature range (550-670°C). As the temperature increases within this range, the predicted volume fraction

of reverted austenite also rises, with the fraction of martensite and austenite approaching equal at around 610°C.

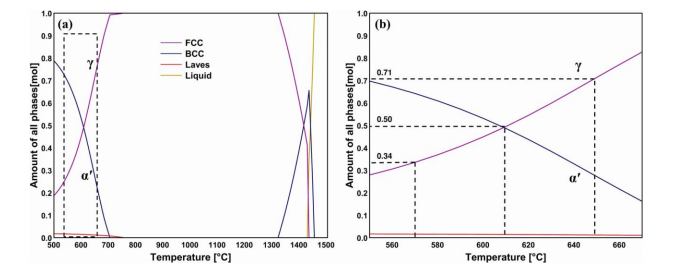


Fig. 2. (a)Calculated equilibrium phase diagram of the experimental steel by Thermo-Calc software; γ : austenite; α ': martensite. (b) Close-up view of (a).

Fig. 3(a) shows a color metallographic image of the experimental steel after solution treatment at 1050°C, captured via optical microscopy. The bright regions correspond to δ -ferrite, with a volume fraction quantified at 11.7%, while the dark regions represent martensite, accounting for 88.3%, which formed directly during cooling from the austenitic temperature range. Fig. 3(b) presents the band contrast map and phase map of the S1050 specimen. δ-ferrite appears as elongated structures tens of micrometers long or as ~10 µm granular features around martensite. The martensite exhibits a lath morphology with widths typically in the range of a few micrometers. Small amounts (<1%) of residual austenite (red regions) are found between the martensitic laths. Fig. 3(c)-(e) display the microstructures of the ST specimens. tempering, the martensitic laths significantly finer, as observed under SEM, while δ-ferrite distribution remained similar to that in S1050. A key difference is the significant formation of reverted austenite between martensite laths in the ST specimens. Reverted austenite grain sizes, measured using AZtecCrystal and calculated as geometric means, reached $1.06\,\mu m$ in ST570, $1.04\,\mu m$ in ST610, and 0.99 µm in ST650. Additionally, ST570 and ST610 exhibited more blocky austenite than ST650, though ST570 had a lower overall austenite density than the other two.

Fig. 3(f) presents the XRD profiles of all specimens. No diffraction peaks corresponding to the austenite phase were detected in the S1050 specimen, indicating that the residual austenite content after solution treatment was extremely low and below the detection limit. In contrast, distinct austenite peaks appeared in the XRD patterns of the three critically tempered specimens. Austenite volume fractions were quantified via Rietveld refinement using Maud software, with all Rwp values—an indicator

the 20% fitting quality—below threshold recommended by Kisi^[22]. Rwp reflects the agreement between calculated and experimental diffraction patterns. Austenite contents in the ST570, ST610, and ST650 specimens were found to be 19.6%, 24.7%, and 18.2%, respectively. Considering the equilibrium predictions shown in Fig. 2(b) at 570°C, 610°C, and 650°C, it is evident that during cooling after critical tempering, a portion of the reverted austenite underwent a secondary martensitic transformation. Moreover, as the tempering temperature increased, a larger fraction of the initially formed austenite reverted back to martensite. Therefore, the actual austenite content in the ST specimens initially increased and then decreased with increasing tempering temperature, deviating from the monotonic increase predicted under equilibrium conditions. Additionally, the austenite grains that underwent secondary transformation tended to grow larger before transforming, which explains the smaller average grain size and the reduced amount of blocky austenite observed in the ST650 specimen.

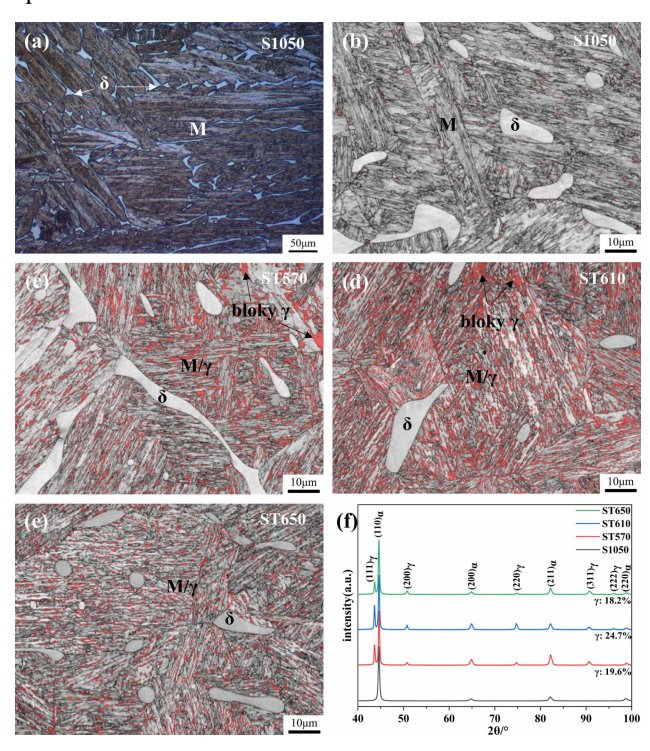


Fig. 3. (a)Color metallographic of S1050. Band contrast (BC) maps and phase maps for (b)S1050, (c)ST570, (d)ST610 and (e)ST650; δ-ferrite; M-martensite; γ-austenite (red part). (f) XRD profiles of all specimens.

3.2 mechanical properties

Fig. 4(a) and Table 2 present the engineering stress-strain curves and mechanical properties of S1050, ST570, ST610 and ST650 specimens. All specimens exhibited continuous yielding behavior. The yield strength (YS) of

each specimen was determined using the 0.2% offset method per Chinese Standard GB/T 228.1-2021. For the S1050 specimen, the 0.2% yield strength was approximately 698 MPa, and the ultimate tensile strength (UTS) reached about 1042 MPa. The yield ratio (YR, defined as YS/UTS) was calculated to be 0.65. This specimen exhibited the lowest uniform elongation (UE) and total elongation (TE), measured at approximately 4.1% and 17.5%, respectively. To comprehensively evaluate the mechanical performance, the product of strength and elongation (PSE) was calculated. The S1050 specimen demonstrated the lowest PSE value of 18.2 GPa.%, which was significantly lower than those of the ST series specimens (ranging from 21.5 to 24 GPa.%), highlighting the enhancement in the strength-ductility synergy achieved through critical tempering treatments.

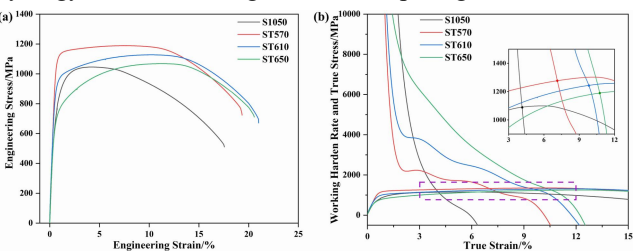


Fig. 4. Tensile stress-strain curves for S1050, ST570, ST610 and ST650 specimens: (a) Engineering stress-strain curves, and (b) True stress-strain and working hardening rate curves.

Table 2.Mechanical properties of the specimens with various treatment states.

Speci	YS/M	UTS/	UE/%	TE/%	YR	PSE/GP
mens	Pa	MPa				a·%
S105	698±	1042±	4.1±0.	17.5±	0.65	18.2
0	8	6	2	0.8		
ST57	1075	1184±	7.1±0.	$19.3 \pm$	0.91	22.8
0	±10	7	4	0.5		
ST61	871±	1125±	9.8±0.	21.0±	0.77	23.6
0	25	13	3	0.7		
ST65	640±	$1068 \pm$	$10.7 \pm$	$20.5 \pm$	0.60	21.9
0	8	11	0.6	0.9		

After critical tempering treatment, the UE of the ST series specimens increased to ~7.1%, ~9.8%, and ~10.7%, respectively. The plasticity increased with the rise in tempering temperature, surpassing that of S1050 (~5.1%) by 40% to 100%. The reverse transformation of austenite during tempering played a key role in enhancing plasticity. The YS of ST570 and ST610 increased to ~1075 MPa and ~871 MPa, respectively, while the UTS improved to ~1184 MPa and ~1125 MPa, and the YR

rose to 0.91 and 0.77. However, the YS of ST650 decreased to ~640 MPa, with the UTS at ~1068 MPa, and the YR dropped to 0.60. As the tempering temperature increased, the strength and the YR of the ST series specimens decreased. The PSE values of the ST specimens all exceeded 20 GPa·%, showing an improvement of over 20% compared to the S1050 specimens, with the highest PSE of 23.6 GPa·% achieved by ST610, demonstrating the best strength–ductility balance.

The working hardening rate (WHR) curve and true stress-strain curves are plotted in Fig.4(b). The WHR curve was derived by differentiating every twenty data points on the true stress-strain curve to minimize noise. When the true strain (ε_T) is less than 2%, all specimens show a rapid WHR decrease due to the deformation of the soft phase (such as δ -ferrite or austenite) and dislocation movement^[23]. For S1050, the WHR curve intersects the true stress curve at the necking point as ε_T increases. The ε_T value at this point is approximately 4.1%, which is equal to the value of UE^[24]. For the ST series specimens, WHR increases with the rise in tempering temperature, and ε_T value at the necking point gradually increases, consistently exceeding that of the S1050 specimen. This is in agreement with the description of UE in Table 2, indicating that the ST series specimens exhibit better work hardening ability and higher toughness during the later stages of tensile deformation compared to the S1050 specimen. For ST570 and ST610, the decline in WHR noticeably decelerates at $\varepsilon_T \approx 2\%$, with the curve becoming relatively flat until necking. In ST650, this deceleration begins earlier in the tensile process and proceeds more gradually. The slower WHR reduction observed in the ST specimens is attributed to the TRIP (Transformation Induced Plasticity) effect induced by the reverted austenite^[25]. Variations in the mechanical stability of austenite among the specimens lead to differences in the activation stages of the TRIP effect, which in turn influence the strength and tensile ductility exhibited by the materials^[26].

3.3 Corrosion Resistance Performance Test

To investigate the effect of tempering temperature on the corrosion resistance of the tested steel specimens, immersion and polarization curve tests were conducted as shown in Fig. 5. In Fig. 5(a), the pitting corrosion pits formed on the surface of the tempered specimens are generally larger than those on the S1050 specimen. ST570 exhibits densely distributed pits smaller than 100 μm, whereas ST610 and ST650 show fewer but

larger pits, ranging from 300 to 500 μ m. As the tempering temperature increases, the diameter of the corrosion pits grows, while pit density initially decreases and then increases, indicating localized corrosion behavior. Fig. 5(b) shows the polarization of the specimens in 3.5 wt.% NaCl solution. All specimens exhibit a passivation region between the self-corrosion potential ($E_{\rm corr}$) and the pitting potential ($E_{\rm pit}$), where the corrosion current rate slows down, indicating that all the test steels possess some degree of corrosion resistance. S1050 shows the highest $E_{\rm corr}$ at -277mV_{SCE}, while $E_{\rm corr}$ values for ST570, ST610, and ST650 are -307mV_{SCE}, -318mV_{SCE}, and -336 mV_{SCE}, respectively. The self-corrosion potential of the specimens decreases as the tempering temperature increases.

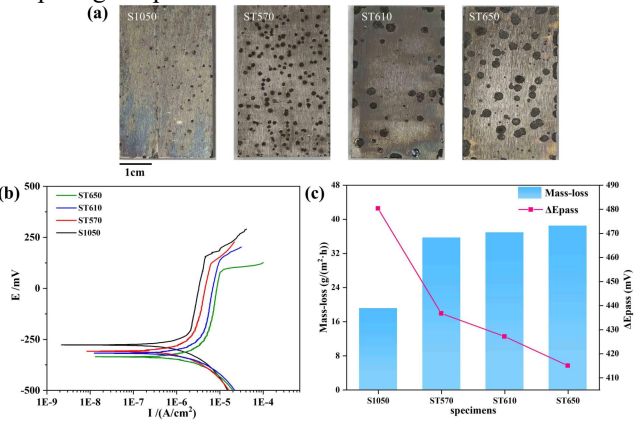


Fig. 5. (a) The surface of the specimens after being soaked in ferric chloride hydrochloric acid solution at 50°C for 24 hours; (b) Polarization curves of the specimens in 3.5 wt.% NaCl solution; (c) The mass loss rate during the immersion test and the passivation region width of the specimens.

Fig. 5(c) summarizes the weight loss rates and the $\Delta E_{\rm pass}$ values of the specimens after the immersion test, as corresponding to Fig. 5(b). The weight loss rate is calculated according to Eq. 1, where m_0 and m_1 are the initial and final weights of the specimens, S is the surface area of the specimen, and t is the immersion time (24 h). $\Delta E_{\rm pass}$ represents the difference between $E_{\rm pit}$ and $E_{\rm corr}$, which reflects the width of the passivation region. It is a key indicator for evaluating the corrosion resistance of stainless steel^[27].

Mass-loss =
$$\frac{m_0 - m_1}{S \cdot t}$$
 (Eq. 1)

As shown in Fig. 5(c), after tempering treatment, the weight loss rate of the specimens increased from 19.1 g/(m²·h) for the S1050 specimen to 35.5~38.5 g/(m²·h), and the passivation region width ($\Delta E_{\rm pass}$) decreased from 480 mV_{SCE} to 415~435 mV_{SCE}. This indicates that tempering treatment reduces the corrosion resistance of the test steels. As the tempering temperature increases, the weight loss rate of the specimens rises, and the

passivation region width (ΔE_{pass}) decreases. Additionally, Fig. 5(a) reveals that after immersion, the pitting corrosion on ST650 exhibits larger pit diameters and a higher quantity of pits. These results suggest that excessive tempering temperatures significantly impair the corrosion resistance of the steel.

4. Discussion

4.1 The stability of reverted austenite

The reverted austenite formed during the critical tempering of the experimental steel has a profound impact on its performance. Fig. 6(a) presents the calculated chemical composition of the reverted austenite at different tempering temperatures. As the temperature increases, enrichment of ferrite-stabilizing elements such as Cr and Si occurs, whereas the concentrations of austenite-stabilizing elements like Ni and Mn show a decreasing trend. Austenite composition strongly influences its stability, including both thermal and mechanical aspects. Thermal stability determines the extent of martensitic transformation during cooling, whereas mechanical stability governs the degree of strain-induced transformation during tensile deformation.

In Fig. 2(b), the predicted equilibrium volume fraction of austenite increases with the rise in tempering temperature, from 34% at 570°C to 71% at 650°C. However, this significantly exceeds the actual austenite contents measured by XRD in the ST specimens (18%-25%), due to partial retransformation of the reversed-transformed austenite into martensite during post-tempering cooling. The retained austenite fraction measured by XRD reflects the final state after cooling. Fig. 6(b) compares the predicted equilibrium fractions with the experimentally measured values. At 570 °C, approximately 53% of the austenite was retained after cooling (decreasing from 34.1% to 18.2%). This retention increased to 59% at 610 °C but dropped markedly to 28% at 650 °C, indicating that a higher tempering temperature promotes secondary martensitic transformation. Additionally, based on the compositional data in Fig. 6(a), the martensite start temperature (M_s) of the austenite at different tempering temperatures was calculated using the empirical equation proposed by Barbier^[28]:

$$M_{\rm S}$$
= 545 - 601.2 × [1 - exp(1 - 0.868C)] - 34.4Mn
- 13.7Si - 9.2Cr - 17.3Ni - 15.4Mo +10.8V +
4.7Co - 1.4Al - 16.3Cu - 361Nb - 2.44Ti -
3448B (Eq. 2)

Fig. 6(b) shows that the Ms temperature increases with rising tempering temperature, indicating that the thermal

stability of austenite decreases as a result of elemental partitioning at higher tempering temperatures. Consequently, reverted austenite formed at elevated temperatures becomes more susceptible to martensitic transformation during subsequent cooling. As a result, the retained austenite content in the final microstructure does not vary monotonically with tempering temperature. This phenomenon also explains why the highest austenite content after critical tempering was achieved at 610°C.

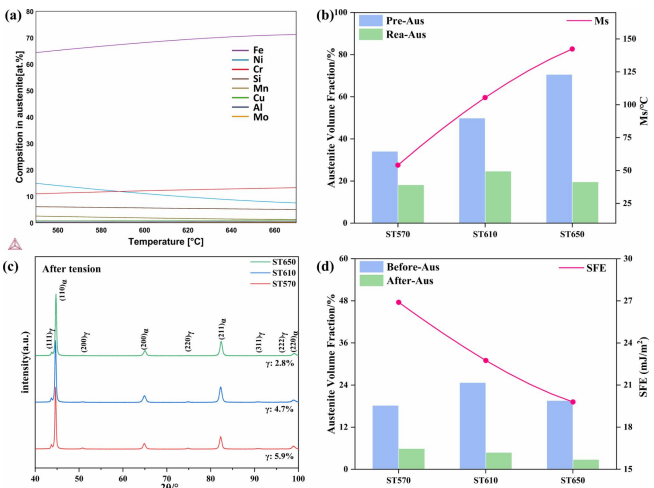


Fig. 6. (a)Calculated chemical composition of reverted austenite as a function of temperature; (b) Calculated Ms temperature of reverted austenite based on the composition from (a), as well as the predicted and the real austenite volume fraction of ST specimens; (c)XRD profiles of ST specimens after tensile test; (d) Calculated SFE of reverted austenite based on the composition from (a), as well as the austenite volume fraction of ST specimens before and after tensile test.

The tensile ductility and strength of martensitic stainless steels containing austenite are significantly affected by specific deformation mechanisms, notably the transformation-induced plasticity (TRIP) effect and twinning-induced plasticity (TWIP) effect. Both mechanisms involve phase transformation or structural changes of the austenite phase under applied stress or strain and are primarily determined by the mechanical stability of austenite. As a face-centered cubic (FCC) phase, the deformation behavior and mechanical properties of austenite are strongly dependent on its stacking fault energy($\gamma_{\rm SFE}$)^[29]. Accordingly, mechanical stability of austenite can be assessed by calculating its γ_{SFE} value, based on the classical Olson–Cohen thermodynamic model^[30,31]:

$$\gamma_{\rm SFE} = 2\rho \Delta G^{\gamma \to \varepsilon} + 2\nu \qquad (Eq. 3)$$

$$\rho = \frac{4}{\sqrt{2}} \cdot \frac{1}{-2 N} \qquad (Eq. 4)$$

Here, ρ denotes the molar surface density of the (111) plane, calculated as 2.96×10^{-5} mol/m² based on Eq. 4, where *a* is the lattice parameter of austenite (3.60 Å) and

 $N_{\rm A}$ is Avogadro's number. The parameter ν , representing the FCC/HCP interfacial energy, is estimated to be ~8 mJ/m² from recent *ab initio* calculations in the Fe–Cr–Ni system^[32]. $\Delta G^{\gamma \to \varepsilon}$ refers to the driving force for the phase transformation from austenite to ε -martensite, which is determined by the chemical composition of the austenite. The driving force can be calculated based on the elemental compositions shown in Fig. 6(a), following the methodology proposed by S. Curtze^[33].

Fig. 6(c) presents the XRD profiles of the ST specimens after tensile testing, with austenite fractions quantified via Rietveld refinement using Maud software. Fig. 6(d) illustrates the changes in austenite content before and after deformation. All ST specimens exhibited a marked reduction in austenite content (less than 6% remaining), indicating significant TRIP effects during deformation, which contributed to improved tensile ductility. The fraction of austenite transformed during tensile deformation varied among the ST specimens: approximately 69% of austenite transformed in ST570, while higher transformation ratios of 81% and 86% were observed in ST610 and ST650, respectively. This suggests that the austenite in ST570 exhibited the highest mechanical stability. The calculated stacking fault energy (SFE) values showed a consistent trend, decreasing from 27 mJ/m² to 20 mJ/m² across the ST specimens, attributable to variations in the chemical composition of the austenite phase. During tensile deformation, austenite with lower mechanical stability tended to transform earlier under deformation, leading to premature yielding and a reduction in yield strength^[34]. As a result, ST650, which had a lower SFE than ST570 and ST610, exhibited earlier yielding and correspondingly lower yield strength.

4.2 Microstructure evolution and deformation mechanisms

The multiple phase transformations occurring during the critical tempering process significantly influence the final microstructure of the specimens, thereby influencing their overall performance. The formation of reverted austenite and the subsequent transformation of unstable austenite during tempering affect the dislocation structure and grain boundary density within the microstructure. Fig. 7 presents the KAM maps and GB distribution maps for the solution-treated specimen (S1050) and the ST series specimens at various tempering temperatures. The geometrically necessary dislocations (GND) in the specimens can be calculated using Eq. 5, where KAM_{ave} represents the geometric mean of the KAM values of the pixels within the statistical region, minimizing the influence of outlier values^[35,36]. KAM_{ave} values for five

martensite and ferrite regions in the microstructure were computed to determine the corresponding GND densities, as shown in Fig. 8(a). Fig. 8(b) presents the grain boundary density at various misorientation angles for each specimen. The grain boundary density was calculated as the ratio of the length of grain boundaries at a given misorientation angle to the area of the measured region.

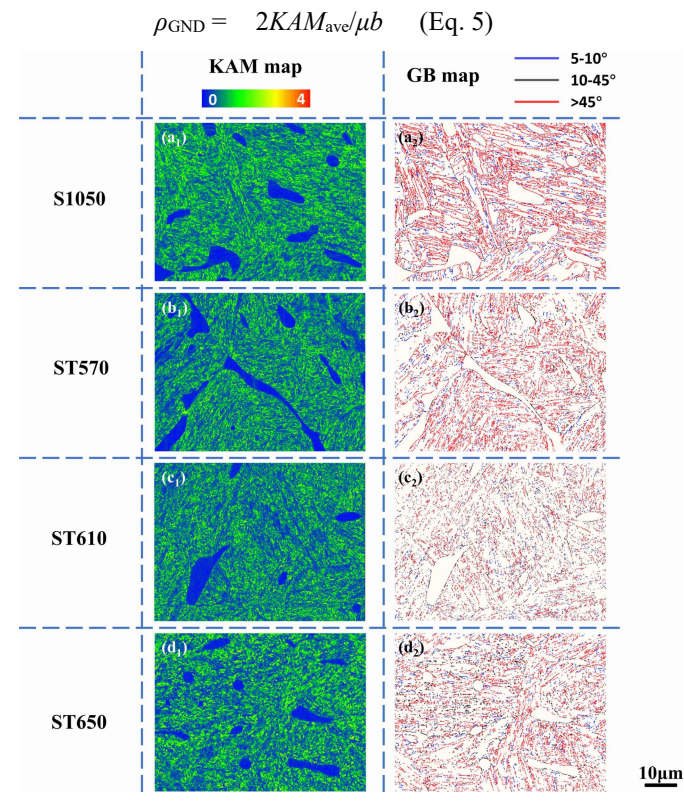


Fig. 7. Kernel average misorientation (KAM) maps (a_1,b_1,c_1,d_1) , and grain boundary (GB) distribution maps (a_2,b_2,c_2,d_2) for S1050,ST570,ST610 and ST650 specimens.

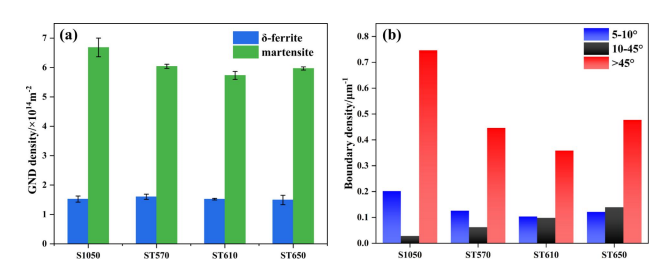


Fig. 8. (a) GND density and (b) grain boundary density of the specimens corresponding to Fig. 7.

There is a clear difference in GND density between the ferrite and martensite phases across all the specimens. Ferrite exhibits a much lower dislocation density than martensite, indicating it is the softer phase, while the strength is primarily provided by martensite. The dislocation density in ferrite remains relatively unaffected by tempering treatments, whereas more pronounced changes occur in the martensite phase. The

higher dislocation density in S1050 corresponds to higher strength and lower tensile ductility, which can be attributed to stress concentration during the tensile deformation. In contrast, precipitation phases and reverted austenite formed during tempering in the ST specimens have a more significant effect on both strength and ductility, leading to improved mechanical performance. As the tempering temperature increases, the dislocation density initially decreases and then increases. The prevailing view is that recovery during tempering leads to the annihilation of dislocations with opposite signs, thereby reducing dislocation density. However, the abnormal increase in dislocation density observed in ST650 martensite is likely due to the formation of secondary martensite from unstable austenite, which introduces additional dislocations and outweighs the effect of recovery. Compared to the higher GND density in S1050, the lower GND density in the ST specimens facilitates more coordinated deformation between martensite and ferrite. The anomalous increase in dislocation density in ST650 contributes to its reduced ductility relative to ST610^[37].

Fig. 8(b) shows the grain boundary density distribution for all the specimens. The grain boundaries are categorized according to interface angle into three groups: 5°~10°, 10°~45°, and >45°, with boundaries greater than 10° classified as high-angle grain boundaries, which can influence mechanical properties^[38]. The overall trend in grain boundary density follows the same pattern as the GND density, reflecting the synergistic effect of tempering treatment on dislocation and grain boundary densities. Boundaries between ferrite and martensite are mostly in the 10°~45° range, while >45° boundaries are prevalent between martensitic laths. The influence of grain boundaries on mechanical behavior is primarily mediated through their effect on the martensitic phase. In ST650, the density of high-angle boundaries increases due to secondary martensite formation; however, this does not substantially enhance strength. Therefore, it can be concluded that neither dislocation strengthening nor grain boundary strengthening plays a dominant role in determining the yield strength of the ST specimens.

The increase in yield strength of ST570 compared to S1050 is primarily attributed to the formation of Laves phases^[39,40] and nanoscale austenite phases^[26] within the microstructure. Precipitation hardening contributes more to strength enhancement than dislocation or grain boundary strengthening. Fig. 9 shows bright-field TEM images of various phases in the ST570 specimen after tensile testing.

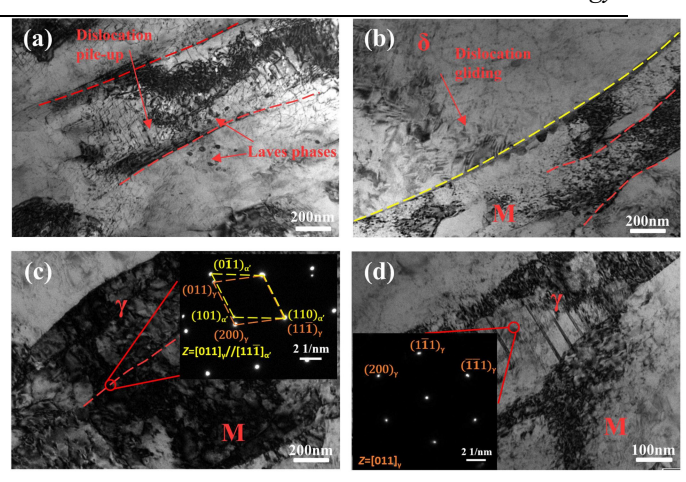


Fig. 9. Bright field TEM images of martensite(a), ferrite(b) after tensile test, and Bright field TEM images and selected area electron diffraction (SAED) image of austenite and martensite (c,d) after tensile test.

In Fig. 9(a), Laves phase precipitates, typically tens of nanometers in size, are observed within the martensitic matrix. Dislocations are entangled around these precipitates, which impede further dislocation motion and play a crucial role in increasing the yield strength. Fig. 9(b) shows the deformed ferrite phase, which initially has a lower dislocation density than martensite, resulting in fewer nucleation sites for precipitates; hence, no precipitates are observed. As the softer phase, ferrite mainly accommodates strain during tensile deformation, leading to dislocation accumulation near phase boundaries. These accumulated dislocations generate back stress, which hardens the ferrite and alleviates strain incompatibility and stress concentration between soft and hard phases, thereby contributing to overall mechanical performance^[8,41]. Fig. 9(c, d) illustrate the behavior of austenite during deformation. As previously discussed, austenite transforms into martensite via the TRIP effect. Fig. 9(c) shows the Kurdjumov-Sachs (K-S) orientation relationship between austenite and strain-induced martensite, observed in a high-dislocation-density region, indicating that localized stress concentration triggered the transformation. Fig. 9(d) reveals another deformation feature in the austenite phase (confirmed by SAED) where nanoscale twinning bands—tens of nanometers wide—form perpendicular to the phase boundary. This observation suggests the occurrence of the TWIP effect in reverted austenite. Strain-induced twinning reduces the effective dislocation slip distance and alters grain orientation, promoting coordinated deformation and thereby enhancing both strength and ductility. [42,43].

As illustrated in Fig. 10, we briefly discuss the deformation mechanism of the ST570 specimen steel during the tensile test. Prior to deformation (Fig. 10(a)),

the microstructure consists of softer ferrite with low GND density and harder martensite with high GND density. The martensite also contains reverted austenite and precipitates distributed between the laths. During tensile loading (Fig. 10(b)), the GND density between martensitic laths increases significantly, indicating strain concentration in these regions. This triggers the synergistic activation of TRIP and TWIP effects in the inter-lath austenite, which together enhance strain accommodation. Notably, this cooperative deformation mechanism occurs earlier in the ST650 specimen and contributes to its premature yielding. Simultaneously, dislocations in the ferrite phase are activated and accumulate at phase boundaries, generating back stress that helps relieve stress concentration. At the necking stage (Fig. 10(c)), dislocations continue to accumulate between martensitic laths, while most of the reverted austenite is transformed due to ongoing TRIP effects. In ferrite, dislocations gather at grain boundary regions, forming subgrain boundaries. These subgrains may rotate, further promoting strain compatibility and delaying crack initiation. Ultimately, cracks nucleate in GND-rich martensitic regions and at ferrite-martensite interfaces, leading to final fracture.

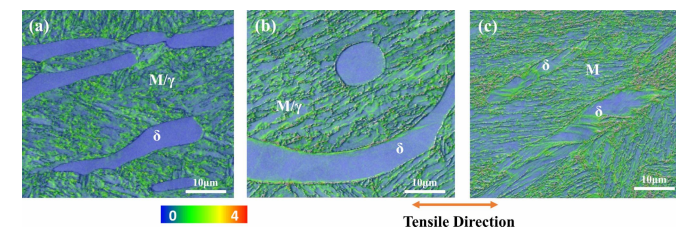


Fig. 10. Band Contrast (BC) maps and kernel average misorientation (KAM) maps for ST570 specimens before tensile test(a), at yield(b), at necking(c).

4.3 Cr inhomogeneity accelerates corrosion

We now discuss the corrosion behavior of the experimental steel. Fig. 11 shows SEM images of micron-scale corrosion pits in the ST570 specimen. These corrosion pits appear at the martensite/austenite composite (M+ γ) laths and at phase boundaries, while no corrosion damage is observed within the ferrite (δ) phase. Fig. 11(b) provides a magnified view of corrosion at a phase boundary, where pits propagate along the interface, leading to selective dissolution of the martensite phase, while the ferrite remains largely unaffected. Chromium (Cr), a key element in enhancing corrosion resistance, contributes to the formation of a protective passive film on stainless steel surfaces^[44–46]. Fig. 12(a₁, b₁) show EBSD band contrast maps of the ST570 and ST650

specimens, with red lines traversing M+ γ and δ regions. Cr concentration along these lines was analyzed via SEM-EDS. A low-pass FFT filter with a DC offset(f<1/7μm⁻¹) was applied to the concentration profile to reduce noise, as shown in Fig. 12(a₂, b₂). The Cr concentration exhibits vatiation within 10~18 wt.%, with its fluctuation pattern corresponding to the M+ γ and δ distribution in the microstructure. Cr is enriched in the δ phase and depleted in the M+y laths, with significant concentration changes at phase boundaries and smaller variations within each phase. Comparatively, the composition fluctuations in ST650 are significantly greater than those in ST570. A distinct Cr-depleted zone is observed at the phase boundary in ST650, where lower and more uneven Cr content is attributed to the enhanced Cr diffusion at higher tempering temperatures.

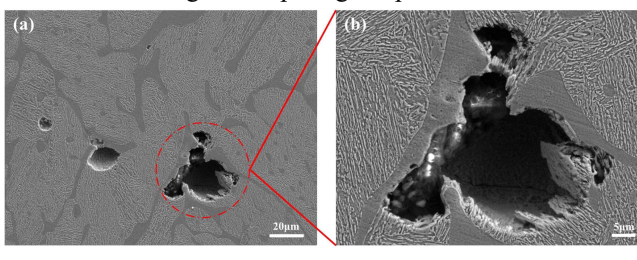


Fig. 11. The SEM image of the surface of the ST570 specimen after immersion corrosion test.

The Cr content at different microstructural locations affects both the thickness and quality of the passive film, which is primarily composed of Cr and Fe oxides. A thicker and less defective passive film offers better resistance to dissolution during corrosion[47,48] . The passive film formed on the M+y lath surface is more susceptible to breakdown, particularly in Cr-depleted regions near phase boundaries. As pitting corrosion initiates, cavities first develop within the M+y laths or at phase boundaries and then expand further within the laths. Once the M+y surrounding a ferrite grain is fully corroded, the ferrite grain may detach, leading to further enlargement of the pit. From an electrochemical standpoint, according to the Cr-depletion theory, Cr-depleted regions act as micro-anodes and undergo preferential dissolution, while Cr-rich regions serve as micro-cathodes and are relatively protected[49]. This micro-galvanic coupling accelerates the dissolution of M+γ laths, particularly at phase boundaries. As the tempering temperature increases, the passive film quality in Cr-depleted boundary regions deteriorates, raising the corrosion loop potential and further accelerating matrix dissolution near these boundaries. Ferrite grains become more easily detached, resulting in larger corrosion pits, as observed in Fig. 5(a) for the ST650 specimen.

Consequently, the corrosion resistance of the ST specimens, indicated by a reduction in the passivation width (ΔE_{pass}) and an increase in mass loss, decreases as the tempering temperature increases.

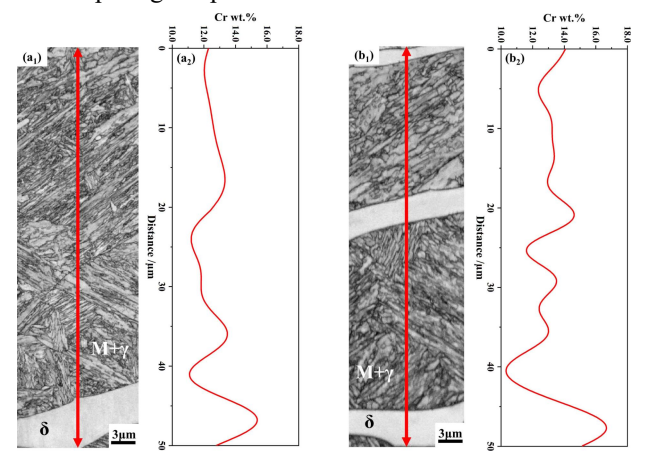


Fig. 12.EBSD map of ST570 specimen(a1) and ST650 specimen(a2); Cr concentration profile of ST570 specimen(b1) and ST650 specimen(b2) after applying a low pass FFT filter(f<1/7μm-1) along the red lines (in a1 and a2).

5 Conclusion

A systematic study was conducted on a novel cast stainless steel containing δ -ferrite, martensite, and reverted austenite to understand the effects of critical tempering treatments. The major findings are summarized as follows:

(1)After solution treatment at 1050°C, the steel exhibited a dual-phase microstructure consisting of approximately 11.7% δ-ferrite and 88.3% martensite. Critical tempering treatments between 570°C and 650°C induced significant formation of reverted austenite. The reverted austenite volume fraction increased with tempering temperature, reaching a maximum at 610°C, before declining at 650°C due to thermal instability and secondary martensitic transformation upon cooling. Moreover, the stability of the reverted austenite was found to be closely associated with its chemical composition and elemental partitioning during tempering.

(2)The stability of reverted austenite played a pivotal role in determining mechanical behavior. Lower SFE, resulting from compositional changes during tempering, enhanced the TRIP effect, thereby improving ductility at the expense of yield strength. The mechanical stability of reverted austenite was temperature-dependent, with optimal stability observed at moderate tempering temperatures (610°C), leading to balanced strength and toughness.

(3)The mechanical behavior was notably enhanced through critical tempering. The ST610 specimen demonstrated superior performance, achieving a YS of

~871 MPa, an UTS of ~1125 MPa, and a TE of ~21.0%, culminating in the highest PSE of ~23.6 GPa·%. This remarkable strength-ductility synergy was attributed to a combination of strengthening mechanisms, including fine laves phase precipitation, stress-induced martensitic transformation (TRIP effect), deformation twinning (TWIP effect), and back-stress hardening arising from heterogeneous microstructures.

(4)Although mechanical properties improved. resistance deteriorated corrosion with increased tempering temperatures. Elevated temperatures promoted chromium segregation at phase boundaries, resulting in the formation of Cr-depleted regions within the multiphase microstructure. These zones acted as preferential sites for localized corrosion initiation, accelerating pit growth, and leading to increased mass loss rates and narrower passivation regions. Especially at 650°C, extensive chromium inhomogeneity further exacerbated the corrosion susceptibility.

Reference:

- [1] C. Wang, Y. Chang, F. Zhou, W. Cao, H. Dong, Y. Weng, M³ microstructure control theory and technology of the third-generation automotive steels with HighStrength and high ductility, Acta Met. Sin 56 (2020) 400. https://doi.org/10.11900/0412.1961.2019.00371.
- [2] S.S.M. Tavares, M.T.G. De Sampaio, G. Perez, B.B. De Almeida, E.A. Ponzio, DL-EPR and AFM study of sensitization of a 17%Cr multiphase stainless steel, Mater. Corros.73(2022)866–875.https://doi.org/10.1002/maco.20 2112814.
- [3] S.S.M. Tavares, I.N. Bastos, J.M. Pardal, T.R. Montenegro, M.R. Da Silva, Slow strain rate tensile test results of new multiphase 17%Cr stainless steel under hydrogen cathodic charging, Int. J. Hydrog. Energy 40 (2015) 16992–16999. https://doi.org/10.1016/j.ijhydene.2015.05.148.
- [4] M. Liu, C. Du, C. Hai, X. Li, Influence of Nb on the hydrogen-assisted cracking behaviour in multiphase stainless steel: Phase fractions, stacking fault energies, and nanosized NbC precipitation, Mater. Sci. Eng. A 903 (2024) 146647. https://doi.org/10.1016/j.msea. 2024.146647.
- [5] M. Liu, S. Huang, Z. Liu, C. Du, Investigations on the passive and pitting behaviors of the multiphase stainless steel in chlorine atmosphere, J. Mater. Res. Technol. 28 (2024) 3365–3375. https://doi.org/10.1016/j.jmrt.2023.12.243.
- [6] Z. Wu, M. Wang, J. He, Y. Liu, H. Zhang, X. Chen, A novel cast multiphase stainless steel with high strength and high toughness, Metall. Mater. Trans. A 54 (2023)

- 2617-2630. https://doi.org/10.1007/s11661-023-07039-3.
- [7] Z. Wu, Y. Liu, H. Zhang, X. Chen, Microstructure and mechanical properties of a novel cast multi-phase stainless steel, J. Mater. Res. Technol. 19 (2022) 4177–4182. https://doi.org/10.1016/j.jmrt.2022.06.138.
- [8] Z. Wu, M. Wang, J. He, X. Chen, Strain partitioning in ferrite and mechanical properties of a cast multiphase stainless steel, Mater. Today Commun. 35 (2023) 105644. https://doi.org/10.1016/j.mtcomm.2023.105644.
- [9] P. Setia, T. Venkateswaran, K.T. Tharian, J. Jain, S.S. Singh, S. Shekhar, Influence of Si content on the microstructure and mechanical properties of silicon stainless steel, Mater. Sci. Eng. A 829 (2022) 142141. https://doi.org/10.1016/j.msea.2021.142141.
- [10] C. Lee, S. Roh, C. Lee, S. Hong, Influence of Si on sigma phase precipitation and pitting corrosion in superaustenitic stainless steel weld metal, Mater. Chem. Phys. 207 (2018) 91–97.https://doi.org/10.1016/j.matchemphys.2017.12.055.
- [11] B.E. Wilde, Influence of silicon on the pitting corrosion resistance of an 18Cr-8Ni stainless steel, Corrosion 42 (1986) 147–151. https://doi.org/10.5006/1.3584894.
- [12] M. Wang, Z. Wu, J He, X. Chen, Microstructure and mechanical properties of a cast TRIP-assisted multiph ase stainless steel, China Foundry 21 (2024) 221–228. https://doi.org/10.1007/s41230-024-3080-3.
- [13] A. Hamada, T. Juuti, A. Khosravifard, A. Kisko, P. Karjalainen, D. Porter, J. Kömi, Effect of silicon on the hot deformation behavior of microalloyed TWIP-type stainless steels, Mater. Des. 154 (2018) 117–129. https://doi.org/10.1016/j.matdes.2018.05.029.
- [14] J. Li, Y. Zhang, W. Jiang, J. Luan, Z. Jiao, C.T. Liu, Z. Zhang, Enhancing work hardening through tuning TRIP by nano-precipitates in maraging stainless steels, Int. J. Plast. 186(2025)104265.https://doi.org/10.1016/j.ijplas.2025.104 265.
- [15] X. Xiong, J. He, H. Zhi, S. Antonov, C. Zhang, Y. Zhong, Y. Su, Optimizing mechanical properties of 15Cr supermartensitic stainless steel by enhanced stability of retained austenite, Mater. Sci. Eng. A 853 (2022). https://doi.org/10.1016/j.msea.2022.143732.
- [16] C. He, G. Xiao, P. Hui, M. Li, L. Tong, Z. Zhang, D. Zou, The new design to improve the stability of retained austenite and mechanical properties in super martensitic stainless steel, Mater. Charact. 217 (2024) 114342. https://doi.org/10.1016/j.matchar.2024.114342.

- [17] Y. Zhao, Z. Zhu, X. Zhao, R. Tian, Y. Lei, P. Yu, H. Peng, L. Chen, Clarify the effect of reversed austenite on the pitting corrosion resistance of super 13Cr martensitic stainless steel, Corros. Sci. 213 (2023) 110992. https://doi.org/10.1016/j.corsci.2023.110992.
- [18] P. Wang, W. Zheng, X. Dai, P. Zhang, Y. Wang, Prominent role of reversed austenite on corrosion property of super 13Cr martensitic stainless steel, J. Mater. Res. Technol. 22 (2023)1753–1767.https://doi.org/10.1016/j.jmrt.2022.12.0 16.
- [19] S.H. Kim, H.K. Moon, T. Kang, C.S. Lee, Dissolution kinetics of delta ferrite in AISI 304 stainless steel produced by strip casting process, Mater. Sci. Eng. A 356 (2003) 390–398. https://doi.org/10.1016/S0921-5093(03)00152-7.
- [20] P. Lichtenegger, R. Bloch, Beitrag zur farbätzung hochlegierter stähle / colour etching of high alloy steels, Pract.Metallogr.12(1975)567–573.https://doi.org/10.1515/ pm-1975-121101.
- [21] F. Van Gen Hassend, S. Weber, Influence of chemical inhomogeneities on local phase stabilities and material properties in cast martensitic stainless steel, Steel Res. Int. 91(2020)1900481. https://doi.org/10.1002/srin.201900481.
- [22] E.H. Kisi, Rietveld analysis of powder diffraction patterns, Mater. Forum 18 (1994) 135–155.
- [23] S. Lee, S. Shin, M. Kwon, K. Lee, B.C. De Cooman, Tensile properties of medium mn steel with a bimodal UFG $\alpha + \gamma$ and coarse δ -ferrite microstructure, Metall. Mater.Trans.A48(2017)1678–1700.https://doi.org/10.1007/s11661-017-3979-z.
- [24] Y. Zhu, X. Wu, Heterostructured materials, Prog. Mater. Sci.131(2023)101019.https://doi.org/10.1016/j.pmatsci.20 22.101019.
- [25] M.-M. Wang, C.C. Tasan, D. Ponge, D. Raabe, Spectral TRIP enables ductile 1.1 GPa martensite, Acta Mater. 111 (2016)262–272.https://doi.org/10.1016/j.actamat.2016.03. 070.
- [26] H.S. Oh, J. Kang, M. Jiang, C.C. Tasan, Role of the nanoscale austenite in micro-strain heterogeneity in PH17-4 martensitic stainless steels, Mater. Sci. Eng. A 895 (2024)146122.https://doi.org/10.1016/j.msea.2024.146122.
- [27] Z. Wang, Z. Feng, L. Zhang, Effect of high temperature on the corrosion behavior and passive film composition of 316 L stainless steel in high H2S-containing environments, Corros.Sci.174(2020)108844.https://doi.org/10.1016/j.cors ci.2020.108844.

- [28] D. Barbier, Extension of the martensite transformation temperature relation to larger alloying elements and c ontents, Adv. Eng. Mater. 16 (2014) 122–127. https://d oi.org/10.1002/adem.201300116.
- [29] G.J.L. Van Der Wegen, P.M. Bronsveld, J.Th.M. De Hosson, A comparison between different theories predicting the stacking fault energy from extended nodes, Scr.Metall.14(1980)285–288.https://doi.org/10.1016/0036-9748(80)90110-6.
- [30] G.B. Olson, M. Cohen, Kinetics of strain-induced martensitic nucleation, Metall. Trans. A 6 (1975) 791–795. https://doi.org/10.1007/BF02672301.
- [31] G.B. Olson, M. Cohen, A mechanism for the strain-in duced nucleation of martensitic transformations, J. Co mmon Met. 28 (1972) 107–118. https://doi.org/10.1016 /0022-5088(72)90173-7.
- [32] R. Li, S. Lu, D. Kim, S. Schönecker, J. Zhao, S.K. Kwon, L. Vitos, Stacking fault energy of face-centered cubic metals: Thermodynamic and *ab initio* approaches, J. Phys. Condens.Matter28(2016)395001.https://doi.org/10.1088/0 953-8984/28/39/395001.
- [33] S. Curtze, V.-T. Kuokkala, Dependence of tensile deformation behavior of TWIP steels on stacking fault energy, temperature and strain rate, Acta Mater. 58 (2010) 5129–5141. https://doi.org/10.1016/j.actamat.2010.05.049.
- [34] Y. Wang, Y. Zhang, W. Gong, X. Rong, S. Harjo, W. Wu, Q. Lu, N. Nakada, Z. Yang, H. Chen, On the r ole of austenite stability in yielding behavior of a me dium mn steel with a duplex austenite-martensite micr ostructure, Acta Mater. 288 (2025) 120840. https://doi.org/10.1016/j.actamat.2025.120840.
- [35] C.-S. Han, H. Gao, Y. Huang, W.D. Nix, Mechanism-based strain gradient crystal plasticity—I. Theory, J. Mech. Phys. Solids 53 (2005) 1188–1203. https://doi.org/10.1016/j.jmps.2004.08.008.
- [36] L.P. Kubin, A. Mortensen, Geometrically necessary dislocations and strain-gradient plasticity: A few critical issues, Scr. Mater. 48 (2003) 119–125. https://doi.org/10.1016/S1359-6462(02)00335-4.
- [37] X. Shang, J. Zhao, X. Li, R.D.K. Misra, X. Wang, X. Xu, C. Shang, The determining role of laminar heterostructures on the mechanical properties of low-density steels, Mater. Sci. Eng. A 881 (2023) 145340. https://doi.org/10.1016/j.msea.2023.145340.
- [38] B.B. Wu, Z.Q. Wang, X.L. Wang, J.X. Zhao, C.J. Shang,

- R.D.K. Misra, Relationship between high angle grain boundaries and hardness after $\gamma \rightarrow \alpha$ transformation, Mater. Sci. Technol. 35 (2019) 1803–1814. https://doi.org/10.1080/02670836.2019.1647936.
- [39] Y. Hu, Y. Niu, Q. Zhang, W. Yang, X. Ma, B. Wang, Synergistic effect of laves phase evolution and porosi ty defects in nuclear-grade FeCrAl alloy laser welded joints: Experiments and crystal plasticity modeling, Op t. Laser Technol. 157 (2023) 108694. https://doi.org/10. 1016/j.optlastec.2022.108694.
- [40] Z. Liu, Z. Yang, X. Wang, J. Liang, Z. Yang, H. Wu, G. Sha, Enhanced strength-ductility synergy in a new 2.2 GPa grade ultra-high strength stainless steel with balanced fracture toughness: Elucidating the role of duplex aging treatment, J. Alloys Compd. 928 (2022) 167135. https://doi.org/10.1016/j.jallcom.2022.167135.
- [41] Y. Zhu, X. Wu, Perspective on hetero-deformation induced (HDI) hardening and back stress, Mater. Res. Lett. 7 (2019) 393–398. https://doi.org/10.1080/21663831.2019.1616331.
- [42] G.C. Kaschner, C.N. Tomé, R.J. McCabe, A. Misra, S.C. Vogel, D.W. Brown, Exploring the dislocation/twin interactions in zirconium, Mater. Sci. Eng. A 463 (2007) 122–127. https://doi.org/10.1016/j.msea.2006.09.115.
- [43] V. Randle, Mechanism of twinning-induced grain boun dary engineering in low stacking-fault energy materials, Acta Mater. 47 (1999) 4187–4196. https://doi.org/10.1 016/S1359-6454(99)00277-3.
- [44] C.L. McBee, J. Kruger, Nature of passive films on iron-chromium alloys, Electrochimica Acta 17 (1972) 1337–1341. ttps://doi.org/10.1016/0013-4686(72)80079-3.
- [45] L.J. Oblonsky, T.M. Devine, A surface enhanced raman spectroscopic study of the passive films formed in borate buffer on iron, nickel, chromium and stainless steel, Corros.Sci.37(1995)17–41.https://doi.org/10.1016/0010-93 8X(94)00102-C.
- [46] K. Oh, I.-H. Toor, S. Ahn, H. Kwon, Effects of Cu on the passive film stability of Fe–20Cr–xCu (x=0, 2, 4wt.%) alloys in H₂SO₄ solution, Electrochimica Acta 88 (2013) 170–176. https://doi.org/10.1016/j.electacta.2012.10.058.
- [47] K. Oh, S. Ahn, K. Eom, K. Jung, H. Kwon, Observation of passive films on Fe–20Cr–xNi (x=0, 10, 20wt.%) alloys using TEM and cs-corrected STEM–EELS, Corros. Sci. 79 (2014)34–40. https://doi.org/10.1016/j.corsci.2013.10.023.
- [48] K. Asami, K. Hashimoto, S. Shimodaira, XPS determination of compositions of alloy surfaces and



surface oxides on mechanically polished iron-chromium alloys,Corros.Sci.17(1977)713–723.https://doi.org/10.1016/0010-938X(77)90067-1.

[49] S. Tokuda, I. Muto, Y. Sugawara, N. Hara, Pit initiation on

sensitized type 304 stainless steel under applied stress: Correlation of stress, cr-depletion, and inclusion dissolution, Corros. Sci. 167 (2020) 108506. https://doi.org/10.1016/j.corsci.2020.108506.